Glioma morphology and tumor-induced vascular alterations revealed in 7 rodent glioma models by in vivo magnetic resonance imaging and angiography

Sabrina Doblas, PhD[1], **Ting He, MS**[1,2], **Debbie Saunders, BS**[1], **Jamie Pearson, BS**[1], **Jessica Hoyle, MS**[3], **Nataliya Smith, PhD**[1], **Megan Lerner, MS**[4], and **Rheal A. Towner, PhD**[1]

[1] Advanced Magnetic Resonance Center, Oklahoma Medical Research Foundation, Oklahoma City, OK, USA

[2] Oklahoma Center for Neuroscience, Oklahoma City, OK, USA

[3] College of Public Health, University of Oklahoma-Tulsa, Tulsa, OK, USA

[4] Department of Surgery, University of Oklahoma Health Science Center, Oklahoma City, OK, USA

Abstract

Purpose—To evaluate the added value of non-contrast-enhanced magnetic resonance angiography (MRA) to conventional MR imaging for a detailed characterization of different rodent glioma models.

Materials and Methods—Intracerebral tumor cell implantation and chemical induction methods were implemented to obtain rat C6, 9L/LacZ, F98, RG2 and ENU-induced glioma models, a human U87 MG tumor model as well as a mouse GL261 glioma model. MR assessments were regularly conducted on a 7 Tesla Bruker BioSpin system. The tumor border sharpness and growth characteristics of each glioma model were assessed from T_2-weighted images. Neovascularization and vascular alterations inherent to each model were characterized by assessing absolute blood volumes, vessel density, length and diameter using Mathematica and Amira software.

Results—9L/LacZ and ENU gliomas both presented flaws that hinder their use as reliable brain tumor models. C6 gliomas were slightly invasive and induced moderate vascular alterations, whereas GL261 tumors dramatically altered the brain vessels in the glioma region. F98, RG2 and U87 are infiltrative models which produced dramatic vascular alterations.

Conclusion—MRI and MRA provided crucial *in vivo* information to identify a distinctive "fingerprint" for each of our 7 rodent glioma models.

Keywords

Glioma; Magnetic resonance Angiography; Peritumoral region; Neovascularization

---

Between 15,000 and 20,000 people are diagnosed each year with a primary malignant brain or central nervous system (CNS) tumor in the United States alone (1). Eighty percent of these tumors are gliomas, i.e. tumors originating from the glial cells of the brain, and especially *Glioblastoma multiforme* (GBM). GBM is the most aggressive glioma type,

Corresponding author: Rheal A. Towner, Oklahoma Medical Research Foundation, 825 NE 13th Street, Oklahoma City, OK, 73104, USA. Phone: (405) 271–7383. Fax: (405) 271–7254. Rheal-Towner@omrf.org.

diagnosed in nearly 10,000 patients each year, and its prognosis is very low. In the best current treatment situation, only 5% of these patients survive the 3-year mark (1). This poor prognosis is due to several factors, such as the resistance to treatment of gliomas and the difficulty in obtaining an early and accurate diagnosis. A clearer understanding of the glioma microenvironment would certainly be crucial for a better diagnosis and an improved patient survival. Indeed, for clinicians to decide on an adequate treatment for the patient, tumor grading must be quick and precise (2), while being virtually non-invasive. From this point of view, non-invasive *in vivo* imaging tools such as magnetic resonance imaging (MRI) and angiography (MRA) are ideal modalities, since they can be used to assess glioma morphology, growth pattern and the angiogenesis process inherent to any tumor type (3). Morphological imaging can particularly provide detailed information on the tissue structure of the glioma and help the assessment of necrosis, which is characteristic of high-grade gliomas and poor prognosis (4). Diffuse infiltration is also interesting to assess, since gliomas are known to exhibit dramatic invasiveness and proliferation as soon as being grade II (5). MRA techniques can follow the vascular alterations brought by the glioma during its progression (6). Neovascularization is an event that distinguishes the moderately aggressive grade III from the GBM-like grade IV tumors (4,7), and the nature of vascular alterations can also inform on the prognosis (8,9). MRA would thus be an interesting imaging modality for the study of gliomas.

We were also highly interested in comparing glioma models varying in their degree of malignancy and provide a characterization for these models as extensive as our MRI methods allow. The models that we chose, from slow-growing ethyl-nitrosourea (ENU)-induced gliomas (10) to more aggressive rodent C6, GL261, 9L/LacZ, RG2 and F98 glioma models, as well as the human U87 glioma model (11), are all considered as good glioma models. However, investigators have underlined the importance of using diverse tumor models during preclinical studies (12), since morphological or biochemical differences between models could potentially result in different treatment responses. It was thus in our interest to characterize these models as precisely as possible, to identify if they really are similar in their growth pattern, morphology and angiogenic behavior. A model of spontaneous chemically-induced gliomas was obtained by exposing pregnant females to ENU, which allowed us to study the transition between low-grade, slow-growing gliomas and high-grade tumors (13). Among the existing glioma cell lines, the C6 model has been widely used as a reliable model of GBM (14) and presenting high similarity with human glioma cells in the expression of genes involved in tumor progression (15). 9L/LacZ (16), F98 (11), GL261 (17) and RG2 (11) cells give rise to more aggressive, infiltrative and angiogenic gliomas. Finally, human U87 cells are considered highly tumorigenic and of high interest for angiogenesis studies (18).

In summary, we used MRI and non-contrast-enhanced MRA techniques to comprehensively characterize diverse glioma models (ENU-induced, C6, F98, 9L/LacZ, GL261, RG2 and U87), as well as to show that these imaging techniques are sufficient to precisely depict glioma behavior *in vivo*.

MATERIAL AND METHODS

Cell Culture and Preparation

Primary rat neocortical astrocytes were kindly obtained from Dr. K. Hensley's group, using the method they developed (19). Briefly, the cortex of 7-day old rat pups was dissected, rinsed and triturated in Ca^{2+}/Mg^+-free Hanks' balanced salt solution. The suspension was centrifuged at 300g for 5 min, then the cell pellet was resuspended in 30 mL of medium (Dulbecco's modified Eagle's medium (DMEM)-F12K supplemented with 10% fetal bovine serum (FBS), 1% L-glutamine and 1% penicillin/streptomycin) and maintained in a 37°C

incubator. The GL261 cell line was kindly provided by Dr. G. Safrany (17) while the other glioma cell lines (rat C6, 9L/LacZ, RG2, F98 and human U87 MG) were purchased from the American Type Culture Collection (ATCC). All cell lines were maintained in a 37°C incubator with 5% CO_2, and cultured in DMEM supplemented with 10% FBS and 1% penicillin/streptomycin (20), at the exception of the human U87 glioma cells which favored Eagle's minimal essential medium (EMEM). Each culture was regularly checked and split when the cell confluence reached 85%.

Before implantation, the cells were briefly trypsinized, centrifuged and resuspended in the corresponding medium. Agarose was added so that the final cell suspension contained 1% ultra-low gelling temperature agarose (Sigma) (20). The cell suspension was regularly shaken to avoid cell sedimentation, and kept in a sterile vial 37°C until implantation.

ENU Exposure

All animal studies were conducted in compliance with our Institutional Animal Care and Use Committee. An 0.1 M solution of ENU was prepared in citric acid and phosphate buffer (pH 6) and administered to 3 pregnant female Fischer 344 rats through the tail vein at 21 days of pregnancy (ENU dose of 50 mg/kg). These conditions have been shown as optimal for the maximal tumor incidence in the Fischer strain by P.E. Kish *et al*. (10). The offspring were naturally delivered and weaned at 22 days old. Only males were selected for the study (n = 17) and kept under weekly observation for any sign of neurological or health problems.

Orthotopic Glioma Models

For the rat glioma cell implantation models (C6 (n = 5), F98 (n = 3), 9L/LacZ (n = 9) and RG2 (n = 5)) as well as the primary rat astrocyte implantation (n = 3), three-month-old male Fischer 344 rats (Charles Rivers Laboratories, Wilmington, MA and Harlan, Indianapolis, IN) were fed a choline-deficient (CD) diet. The cell implantation procedure was conducted based on the method developed by N. Kobayashi *et al.* (21). Briefly, each animal was anesthetized (2.7% isoflurane at 0.7 L/min oxygen) and immobilized on a stereotaxic unit (Stoelting Co., Wood Dale, IL). After disinfection and incision of the skin of the head, a hole was drilled through the skull 2 mm lateral and 2 mm anterior to the bregma, on the right-hand side of the skull. 10^4 rat glioma cells suspended in 10 μL were injected at 3 mm in depth from the dura at a rate of 2 μL/min, using a 25-gauge Hamilton needle mounted on a 25 μL Hamilton glass syringe (Hamilton, Reno, NV). A waiting time of 2 min was implemented following injection. Control injection of rat primary astrocytes were also conducted using the same conditions. The rats implanted with human U87 cells (n = 5) were three-month-old athymic *rnu/rnu* male rats (Charles Rivers Laboratories, Wilmington, MA). The procedure was slightly adapted: 10^5 U87 cells in 10 μL were injected at a rate of 0.8 μL/min, to ensure the least amount of stress possible for these large human cells, and a waiting time of 5 min was then implemented. Finally, 2-month-old C57BL/6 male mice fed a CD diet were implanted with 2×10^4 GL261 cells in 4 μL at 1mm anterior and 2 mm lateral to the bregma, at a depth of 1.5 mm below the dura, using an injection rate of 0.6 μL/min (n = 5) for the mouse glioma model.

MRI and MRA Experiments

Animals were imaged at the Advanced Magnetic Resonance Center of our institution using a 7 Tesla-30 cm horizontal bore magnet (Bruker BioSpin MRI Gmbh, Ettlingen, Germany) 7 days after cell implantation and then every third day until the death of the animal for the orthotopic glioma models. The ENU-exposed rats were imaged at 3 months of age, and subsequently every month until their death. Each animal was anesthetized (1.5% isoflurane at 0.7 L/min oxygen) and placed in a MR probe in a supine position. A head surface coil (Bruker BioSpin MRI Gmbh, Ettlingen, Germany) was used as a signal receiver, and

radiofrequency (RF) pulses were transmitted to the sample through a quadrature volume coil (72 mm inner diameter, Bruker BioSpin MRI Gmbh, Ettlingen, Germany). The respiration rate (typical range: 30–50 breaths/min) of the animals was monitored throughout the whole experiment, using an abdominal pneumatic pillow (SA Instruments, Inc., Stony Brook, NY).

For glioma morphological imaging, T_2-weighted images (24 transverse slices with a thickness of 1 mm and taken in a field of view (FOV) of 3.5×3.5 cm^2, with a matrix size of 256×256 pixels, for a resulting in-plane resolution of 140 μm) were acquired using a RARE (rapid acquisition with relaxation enhancement) sequence, with a repetition time (TR) of 3000 ms and an echo time (TE) of 63 ms, for a total acquisition time of 13 min. Mouse brain morphological images were acquired with a slice thickness of 0.5 mm and a FOV of 2×2 cm^2, for an approximate in-plane resolution of 80 μm.

For the assessment of glioma angiogenic behavior, rat MRA data was acquired using a fast low angle shot (FLASH) 3D method within a volume of interest (VOI) of $2.6 \times 1.7 \times 1.1$ cm^3, at an angle of 5° relative to the horizontal plane, a TE of 2.3 ms, a TR of 25ms and a flip angle of 25°, for a total acquisition time of 27 min. The original data (matrix size of $256 \times 256 \times 128$ and pixel resolution of $102 \times 66 \times 86$ μm^3) were then zero-filled to provide a $512 \times 512 \times 256$ final image matrix, with a pixel resolution of $51 \times 66 \times 43$ μm^3. Mouse MRA data was acquired within a VOI of $1.28 \times 1 \times 0.64$ cm^3, at an angle of 16° relative to the horizontal plane, for a total acquisition time of 25 min, a non-zero filled matrix size of $256 \times 128 \times 64$ and a pixel resolution of $50 \times 78 \times 100$ μm^3.

Determination of Tumor Growth Pattern and Morphology

Several levels of information were extracted from these images, such as the glioma invasiveness and the tumor volume. Using the software ImageJ (v 1.42q, NIH, Bethesda, MD) and based on their brighter appearance, cell-originating gliomas were delineated on the T_2-weighted MR images and their volumes were determined. ENU-induced gliomas were identified from their typical aspect (dark spots surrounded by hyperintense regions, as shown by P.E. Kish *et al.* (10)). Tumor doubling times were calculated after fitting the experimental volume data to a modified Gompertz function (22,23):

$$V(t) = V_0 exp \left[\frac{\beta}{\alpha} (1 - e^{-\alpha t}) \right]$$

[Eq. 1]

The tumor volume V(t) is here described as a function of the initial volume V_0, the tumor specific growth rate α (day^{-1}) and the retardation factor β (day^{-1}). The time needed by the tumor to double in size (doubling time Td (day)) can then be easily determined from [Eq. 1] (6). The general morphology of the glioma as well as the presence and appearance of necrotic areas were noted (characterized by low intensity pixels). To evaluate the morphology of the border between the glioma tissue and its surroundings, the slice presenting the largest tumor surface area was selected and the peritumoral region was divided into 8 ROIs (regions of interest) of equal size. A distribution of signal intensity was acquired in each ROI, perpendicular to the border tumor/healthy tissue, using the "Plot Profile" tool available in the software ImageJ, and the slopes of the intensity profiles were averaged to provide an indication of the glioma border sharpness (a sharp intensity change, i.e. sharp slope, indicated a net border between glioma and healthy brain tissue, whereas a small slope was related to a pronounced glioma infiltration). The peritumoral ROIs crossing a necrotic or edematic region were canceled from the study. Finally, the time of death of each animal as well as the latency time (defined as the number of days needed by the tumor to reach 10 mm^3 or 2 mm^3 in size, for the rat and mouse tumor models respectively) of each tumor was noted.

Blood Volume Quantification and Vessel Measurements

Blood volume quantification was done using a Mathematica-based program (Mathematica 7.0, Wolfram Research, Champaign, IL). A ROI encompassing the medial cerebral artery branching in the tumor area was selected and the number of high intensity pixels (corresponding to flowing blood) was computed to provide us with absolute blood volumes (BV) (6). BV ratios were then calculated for each time point, with the first day of assessment being considered as the baseline for each animal. Co-registration of the T_2-weighted images and the MRA data was conducted using the imaging software Amira (v 4.1.0, Mercury Computer Systems, Chelmsford, MA) by superposing the 2 datasets based on their FOV size and position relative to the magnet isocenter. Finally, vessels were counted and measured to assess the vascular alterations induced by the glioma. Briefly, each vessel proximal to the glioma was labeled, and its diameter and length were estimated using the "3D measuring" tool available in the Amira software.

Histology and Immunohistochemistry

Animals were regularly checked. As soon as precursor signs of death were observed (animal non-responsive, not drinking/eating anymore, presenting porphyrin secretions around its nose and eyes), rats were imaged, kept under anesthesia and cardiac perfused with PBS. Brains were then extracted and fixed by immersion fixation in 10% buffered zinc formalin. Five micron-thick paraffin-embedded sections were stained with hematoxylin and eosin (H&E) or immunostained for vascular endothelial growth factor (VEGF, the main pro-angiogenic factor) (1:400, Thermo Scientific, Fremont, CA).

Statistical Analysis

Statistical analysis of the data was performed using Prism 5.01 (GraphPad software, LaJolla, CA). Survival curves were built on the basis of a Kaplan-Meier curve and their statistical differences were determined using a log-rank (Mantel-Cox) test. Other differences between groups were examined using two-tailed, unpaired, Student's t-tests with Welch's correction. In all cases, significance was considered for tests yielding a p value below 0.05 (*), 0.01 (**) or 0.001 (***).

RESULTS

Determination of Tumor Growth Pattern and Morphology

MR images from the primary astrocyte-implanted rats showed that our implantation procedure did not induce any non-desired effects (Fig. 1A), and only slight inflammation was observed in the tissue (which disappeared one week after the procedure). The C6, GL261 and U87 cell lines as well as the ENU exposure produced slightly invasive gliomas, with a peritumoral region that appeared as a relatively distinct border between the tumor region and the surrounding healthy tissue, as observed on the MR images, the H&E staining (Fig. 1) and the peritumoral signal intensity slopes (Fig. 2). The other glioma models (9L/LacZ, RG2 and F98) appeared as aggressive gliomas that infiltrate the surrounding tissue during tumor growth and progression (Fig. 1 and 2). Small necrotic areas (low intensity regions on T_2-weighted images, and areas of very low/null glioma cell density on H&E images) disseminated throughout the tumor were seen in C6, F98 and 9L/LacZ gliomas, whereas GL261, ENU, RG2 and U87 tumors showed large necrotic centers (Fig. 1).

The ENU-induced gliomas were quickly identified as possessing a specific growth pattern since they were growing very slowly (latency time of 29 ± 5.01 weeks and average Td of 5 ± 1.3 weeks) compared to the models obtained by intracerebral cell implantation, and survived for months (survival time of 36 ± 3 weeks). Rats bearing ENU-induced gliomas often showed multiple tumors (in average, 3 ± 1 gliomas). The latency times of most of the

intracerebral cell implantation models were within the same range (11 ± 1.93 days, 14 ± 5.03 days, 12 ± 2.47 days, 11 ± 1.39 days and 15 ± 6.45 days for the C6, F98, GL261, RG2 and U87 gliomas, respectively). 9L/LacZ tumors distinguished themselves by a relatively longer latency time (25.6 ± 5.9 days) and slower growth (Fig. 3), apparently having some difficulties establishing themselves into the host brain tissue. Within the other orthotopic glioma models, RG2 gliomas had the quickest growth (Fig. 3, Td of 1.52 ± 0.35 days), whereas F98 and U87 tumors had longer survival times (Fig. 3, 25 and 28 days, respectively). However, the growth patterns of the orthotopic tumor models were globally very similar.

Finally, 9L/LacZ and ENU gliomas both presented unreliable and irreproducible growth. In addition to its previously mentioned growth characteristics, 9L/LacZ tumors regularly exhibited spontaneous glioma regression (22%) or absence of tumor growth (33%) in the implanted animals. The ENU model also presented some flaws, since out of the 17 male pups obtained from ENU-injected females, four animals did not appear to have any kind of brain tumors, and in 60% of the cases, other fast-growing tumor types were observed (i.e. ependymomas, meningiomas and peripheral nervous system tumors). It was thus difficult to follow the progression of the ENU gliomas for a satisfactory period of time, since the animals were very often killed by other tumor types before glioma manifestation or progression.

Blood Volume Quantification and Vessel Measurements

The angiogenic behavior exhibited by each glioma model was assessed from quantification of BV and vessel measurements. For comparison, quantification of the tumor ROI BV for rats implanted with primary rat astrocytes (or "CTRL" rats) was used as a sham control baseline. As expected, neither a change in BV (final BV ratio of 0.98 ± 0.075) nor vascular alterations (7% change in vessel length and 7% change in vessel diameter, Fig. 4A and Table 1) were observed for these animals.

Each glioma model possessed its own individual angiogenic behavior, as illustrated by the tumor BV, the 3D vasculature representations and the vessel measurements. C6, F98, RG2, U87 and ENU glioma models underwent a similar increase in BV during tumor progression, with BV ratios ranging from 1.23 ± 0.13 (ENU gliomas) to 1.34 ± 0.25 (U87 gliomas) at the last MRI time point. This last time point occurred approximately at 23 days after cell implantation for the orthotopic implantation models (glioma volumes of 169 ± 63 mm^3 for the rat models and 102 ± 18 mm^3 for the mouse model) and at 30 weeks of age for the ENU induction models (average volume of 53 ± 34 mm^3). The final BV ratios of the C6, F98, 9L/LacZ and RG2 gliomas were 1.26 ± 0.14, 1.25 ± 0.08, 1.51 ± 0.46 and 1.25 ± 0.12, respectively. GL261 gliomas were highly distinguishable from the other models, since they induced a dramatic increase in BV ratios over a relatively short period of time (up until 1.73 ± 0.35 in 2 weeks).

Vessel measurements and vasculature assessment underlined the preference of C6 and F98 glioma models to use the pre-existing blood vessels for their nutrient supply, since no newly generated vessels were observed and since the vessels grew longer (31% increase and 94% increase for C6 and F98 gliomas, respectively) and larger (40% increase for C6 gliomas) in the tumor area (Fig. 4B and Table 1). RG2 tumors distinguished themselves since they did not induce any change in vessel length or diameter on the main vessels, but new blood vessels could be seen in the tumor ROI only 2 weeks after cell implantation (Table 1). Finally, in the 9L/LacZ, GL261 and U87 gliomas, we observed both new blood vessels and a dramatically altered pre-existing vasculature (Fig. 4C, 4D and Table 1). The most obvious case of this adaptation of pre-existing vessels was shown by the GL261 model (up to 83% increase in vessel diameter, Table 1). These models could then be classified as highly

angiogenic, high-grade gliomas compared to the moderately aggressive C6 and F98 tumors. The assessment of VEGF immunostaining assays correlated with these MRA results. C6, F98 and ENU presented a low to moderate level of VEGF expression (Fig. 5B), whereas the tumor models where new feeder vessels were observed (GL261, RG2 and U87) showed a pronounced level of VEGF expression (Fig. 5Cand 5D).

DISCUSSION

Glioma diagnosis must be as accurate and early as possible, to help physicians decide of the best treatment for the patient. In particular, the tumor should be accurately graded (2), since its grade translates its entire behavior. This level of information can be provided by MRI and MRA, which are ideal non-invasive *in vivo* imaging modalities able to provide precise information on tumor morphology and growth pattern (MRI) as well as vascularization behavior (MRA). Most of the parameters assessed during this study (e.g. tumor growth rate and BV) allow to characterize the aggressiveness of the glioma and help tumor grading. For example, endothelial proliferation (vessel density and BV) can distinguish grade III from grade IV astrocytomas (4), and the latency time is thought to reflect the grade of a glioma (24). Vascular alterations are thought to be descriptive of low to moderate-grade gliomas, whereas high-grade tumors prefer to generate new vessels for their needs (8). MR techniques present certain advantages when compared to other invasive diagnosis techniques, such as contrast-enhanced CT (which requires the use of contrast agents and the calculations of parameters such as its extravasation properties to guarantee reliable results) or *ex vivo* immunohistochemistry assays conducted on biopsied tissue samples. Within the MR techniques available to study the vasculature, most investigators favor the use of gadolinium-based (25,26) or iron oxide contrast agents (27). A few groups used a non-contrast MRA approach to visually assess rodent brain vasculature (28–30), but absolute BVs have never been assessed in rat glioma models *in vivo*. Anon-contrast MRA method is a good alternative to contrast-enhanced techniques, and it can be easily implemented to generate absolute BVs, vessel length and diameter measurements and a direct view of the relationships between the tumor and its host tissue. When coupled to a powerful imaging software such as Amira for volume rendering, MRA was able to give detailed information on 3 angiogenesis criteria: the vessel density (7), the blood vessel volume (8) and the presence of vascular alterations (9). Volume rendering and glioma/vasculature coregistration are crucial to study the effect of the tumor on its environment in more details, and in particular on the host vasculature. Indeed, the vessels distal to the tumor did not seem to be affected at all, whereas the proximal ones were subject to dramatic alterations (Fig. 4 and Table 1). One limit of this method is its resolution, since only the main vasculature (> 50 μm) can be assessed, and one could propose a combination of MRA and a contrast-enhanced method to gather information on both levels (main vasculature and capillary bed, respectively). However, assessing the bigger vessels was found to be sufficient to distinguish distinctive angiogenic patterns in 7 rodent glioma models, and non-contrast-enhanced MRA has been showed able to detect the vascular alterations induced by tumors as small as 1 mm^3 in size (31).

An ideal glioma model should closely resemble human GBM in its morphology, invasiveness and angiogenic behavior, to allow clinically relevant studies of tumor behavior and therapeutic drug efficiency. For this purpose, several investigators have proposed a definition for a "good" glioma model (17,32,33). The lack of reproducibility found in both the ENU model and the 9L/LacZ model does not make them good glioma models. As observed in the literature and throughout this study, the aggressive 9L/LacZ gliomas are highly invasive (17) and have extensive neovascularization (16), but their pronounced immunogenicity (11) and the fact that they are classified as gliosarcomas (15) make them a poor choice for glioma studies. This problem can be eliminated by using non-immunogenic

models (e.g. RG2). The chemical induction model via transplacental ENU exposure also lacked reproducibility, since diverse types of tumors were found, some of them with dramatically shorter survival times than the ENU-induced gliomas (e.g. meningiomas (13), spinal cord tumors (13) and other primitive neuroectodermal tumors (34)). However, it is widely recognized that transplacental ENU exposure creates a large variety of nervous system tumors (10,13,34) and the distribution of brain tumors found in our case closely resembled those from the literature (10). However, since no implantation model currently exists for low-grade gliomas, one could use ENU induction to obtain such tumors, but it should be noted that a careful study design would have to be implemented if the investigator desires to assess drug efficiency. Some investigators reported problems of spontaneous regression of the C6 glioma model (35) whereas we never encountered this particular issue and always had reproducible growth of the C6 cell line during our study. Every other orthotopic model (F98, RG2, GL261 and U87) presented moderate to high invasiveness (36), coupled to tumor-induced necrosis and vascular alterations (12), which make them good glioma models (for further therapeutic agent studies, for example).

As noted previously, these tumor models are all considered as good glioma models, which are widely used to mimic human GBM for preclinical studies. However, one should ask themselves if these glioma models can indeed be substituted one for another. Our extensive radiological assessment of morphology, border sharpness and vascularization of a spectrum of rodent glioma models made it possible to identify a distinctive "fingerprint" of each glioma model that distinguished it from the others (Fig. 1, 2, 3, 4, 5 and Table 1). ENU gliomas had a characteristic morphology with large necrotic centers but did not induce major vascular alterations. The C6 glioma model is a moderately aggressive tumor with a distinct peritumoral region and which prefers to alter pre-existing vessels for its growth needs. F98 gliomas resemble C6 tumors, except for their more pronounced invasiveness and vascular alterations. GL261 gliomas had a moderately diffuse peritumoral region, highly necrotic and dramatically altered the vessel diameters in the tumor region. RG2 and U87 tumors had diffuse margins and showed numerous new feeder vessels appearing in 2 weeks. Based on their angiogenic profile, it appears that each glioma model creates its own array of vessels with different diameter and length. This could potentially infer that the nutrient and oxygen transport within each glioma is different between models, as large vessels do not perfuse the tissue as numerous smaller vessels would. The blood flow and transport phenomena are going to differ from one model to another, which is crucial to consider for radio- and chemotherapeutic studies for example, as the delivery of drugs in a patient entirely relies on the state of the vasculature present at time of drug administration (37), and the efficiency of radiotherapy depends on hypoxia level of the targeted tissue (38).

In conclusion, our work brought detailed information on the distinctive morphology and angiogenic behavior of these 7 rodent (C6, F98, 9L/LacZ, GL261, RG2 and ENU) and human (U87) glioma models. This underlines the importance of giving an accurate diagnosis, since gliomas possessing different characteristics can react differently to treatment.

Acknowledgments

References

1. CBTRUS. Statistical report: primary brain tumors in the United States, 2000–2004: Central brain tumor registry of the United States. 2008:1–62.

2. Louis DN, Ohgaki H, Wiestler OD, et al. The 2007 WHO classification of tumours of the central nervous system. Acta neuropathologica. 2007; 114:97–109. [PubMed: 17618441]

3. Plate KH, Breier G, Weich HA, Risau W. Vascular endothelial growth factor is a potential tumour angiogenesis factor in human gliomas in vivo. Nature. 1992; 359:845–848. [PubMed: 1279432]

4. Gudinaviciene I, Pranys D, Juozaityte E. Impact of morphology and biology on the prognosis of patients with gliomas. Medicina (Kaunas). 2004; 40:112–120. [PubMed: 15007269]

5. Furnari FB, Fenton T, Bachoo RM, et al. Malignant astrocytic glioma: genetics, biology, and paths to treatment. Genes Dev. 2007; 21:2683–2710. [PubMed: 17974913]

6. Doblas S, Saunders D, Kshirsagar P, et al. Phenyl-tert-butylnitrone induces tumor regression and decreases angiogenesis in a C6 rat glioma model. Free Radic Biol Med. 2008; 44:63–72. [PubMed: 18045548]

7. Leon SP, Folkerth RD, Black PM. Microvessel density is a prognostic indicator for patients with astroglial brain tumors. Cancer. 1996; 77:362–372. [PubMed: 8625246]

8. Folkerth RD. Descriptive analysis and quantification of angiogenesis in human brain tumors. J Neurooncol. 2000; 50:165–172. [PubMed: 11245275]

9. Korkolopoulou P, Patsouris E, Kavantzas N, et al. Prognostic implications of microvessel morphometry in diffuse astrocytic neoplasms. Neuropathol Appl Neurobiol. 2002; 28:57–66. [PubMed: 11849564]

10. Kish PE, Blaivas M, Strawderman M, et al. Magnetic resonance imaging of ethyl-nitrosourea-induced rat gliomas: a model for experimental therapeutics of low-grade gliomas. J Neurooncol. 2001; 53:243–257. [PubMed: 11718257]

11. Barth RF. Rat brain tumor models in experimental neuro-oncology: the 9L, C6, T9, F98, RG2 (D74), RT-2 and CNS-1 gliomas. J Neurooncol. 1998; 36:91–102. [PubMed: 9525831]

12. Valable S, Lemasson B, Farion R, et al. Assessment of blood volume, vessel size, and the expression of angiogenic factors in two rat glioma models: a longitudinal in vivo and ex vivo study. NMR Biomed. 2008; 21:1043–1056. [PubMed: 18615861]

13. Koestner A, Swenberg JA, Wechsler W. Transplacental production with ethylnitrosourea of neoplasms of the nervous system in Sprague-Dawley rats. Am J Pathol. 1971; 63:37–56. [PubMed: 4323476]

14. Grobben B, De Deyn PP, Slegers H. Rat C6 glioma as experimental model system for the study of glioblastoma growth and invasion. Cell Tissue Res. 2002; 310:257–270. [PubMed: 12457224]

15. Sibenaller ZA, Etame AB, Ali MM, et al. Genetic characterization of commonly used glioma cell lines in the rat animal model system. Neurosurg Focus. 2005; 19:E1–E9. [PubMed: 16241103]

16. Plate KH, Breier G, Millauer B, Ullrich A, Risau W. Up-Regulation of Vascular Endothelial Growth Factor and its Cognate Receptors in a Rat Glioma Model of Tumor Angiogenesis. Cancer Res. 1993; 53:5822–5827. [PubMed: 7694795]

17. Szatmari T, Lumniczky K, Desaknai S, et al. Detailed characterization of the mouse glioma 261 tumor model for experimental glioblastoma therapy. Cancer science. 2006; 97:546–553. [PubMed: 16734735]

18. Cheng SY, Huang HJ, Nagane M, et al. Suppression of Glioblastoma Angiogenicity and Tumorigenicity by Inhibition of Endogenous Expression of Vascular Endothelial Growth Factor. Proc Natl Acad Sci U S A. 1996; 93:8502–8507. [PubMed: 8710899]

19. Hensley K, Abdel-Moaty H, Hunter J, et al. Primary glia expressing the G93A-SOD1 mutation present a neuroinflammatory phenotype and provide a cellular system for studies of glial inflammation. J Neuroinflammation. 2006; 3:2–10. [PubMed: 16436205]

20. von Kienlin M, Ziegler A, Le Fur Y, Rubin C, Decorps M, Remy C. 2D-spatial/2D-spectral spectroscopic imaging of intracerebral gliomas in rat brain. Magn Reson Med. 2000; 43:211–219. [PubMed: 10680684]

21. Kobayashi N, Allen N, Clendenon NR, Ko LW. An improved rat brain-tumor model. J Neurosurg. 1980; 53:808–815. [PubMed: 7003068]

22. Rygaard K, Spang-Thomsen M. Quantitation and Gompertzian analysis of tumor growth. Breast Cancer Res Treat. 1997; 46:303–312. [PubMed: 9478282]

23. Demicheli R, Foroni R, Ingrosso A, Pratesi G, Soranzo C, Tortoreto M. An exponential-Gompertzian description of LoVo cell tumor growth from in vivo and in vitro data. Cancer Res. 1989; 49:6543–6546. [PubMed: 2819710]

24. Johansson FK, Goransson H, Westermark B. Expression analysis of genes involved in brain tumor progression driven by retroviral insertional mutagenesis in mice. Oncogene. 2005; 24:3896–3905. [PubMed: 15750623]

25. Schierling W, Troidl K, Mueller C, et al. Increased intravascular flow rate triggers cerebral arteriogenesis. J Cereb Blood Flow Metab. 2009; 29:726–737. [PubMed: 19142189]

26. Seshadri M, Ciesielski MJ. MRI-based characterization of vascular disruption by 5,6-dimethylxanthenone-acetic acid in gliomas. J Cereb Blood Flow Metab. 2009; 29:1373–1382. [PubMed: 19458603]

27. Lin CY, Lin MH, Cheung WM, Lin TN, Chen JH, Chang C. In vivo cerebromicrovasculatural visualization using 3D DeltaR2-based microscopy of magnetic resonance angiography (3DDeltaR2-mMRA). Neuroimage. 2009; 45:824–831. [PubMed: 19154792]

28. Kitamura N, Araya R, Kudoh M, et al. Beneficial effects of estrogen in a mouse model of cerebrovascular insufficiency. PLoS One. 2009; 4:e5159. [PubMed: 19357782]

29. Cheng CH, Kikuchi T, Chen YH, et al. Mutations in the SLC2A10 gene cause arterial abnormalities in mice. Cardiovasc Res. 2009; 81:381–388. [PubMed: 19028722]

30. Togbe D, de Sousa PL, Fauconnier M, et al. Both functional LTbeta receptor and TNF receptor 2 are required for the development of experimental cerebral malaria. PLoS One. 2008; 3:e2608. [PubMed: 18612394]

31. Bullitt E, Wolthusen PA, Brubaker L, Lin W, Zeng D, Van Dyke T. Malignancy-associated vessel tortuosity: a computer-assisted, MR angiographic study of choroid plexus carcinoma in genetically engineered mice. AJNR Am J Neuroradiol. 2006; 27:612–619. [PubMed: 16552004]

32. Barth, RF.; Moeschberger, ML. Rat brain tumor models and the statistical evaluation of survival data in experimental neuro-oncology. In: Chiocca, EA.; Breakefield, XO., editors. Gene therapy for neurological disorders and brain tumors. Totowa, NJ: Humana Press; 1997. p. 313

33. Peterson DL, Sheridan PJ, Brown WE Jr. Animal models for brain tumors: historical perspectives and future directions. J Neurosurg. 1994; 80:865–876. [PubMed: 8169627]

34. Vaquero J, Coca S, Zurita M, et al. Synaptophysin expression in "ependymal tumors" induced by ethyl-nitrosourea in rats. Am J Pathol. 1992; 141:1037–1041. [PubMed: 1443043]

35. Vince GH, Bendszus M, Schweitzer T, et al. Spontaneous regression of experimental gliomas--an immunohistochemical and MRI study of the C6 glioma spheroid implantation model. Exp Neurol. 2004; 190:478–485. [PubMed: 15530886]

36. Asanuma T, Doblas S, Tesiram YA, et al. Visualization of the protective ability of a free radical trapping compound against rat C6 and F98 gliomas with diffusion tensor fiber tractography. J Magn Reson Imaging. 2008; 28:574–587. [PubMed: 18777527]

37. Acker T, Plate KH. Role of hypoxia in tumor angiogenesis-molecular and cellular angiogenic crosstalk. Cell Tissue Res. 2003; 314:145–155. [PubMed: 12898211]

38. Yasuda H. Solid tumor physiology and hypoxia-induced chemo/radio-resistance: novel strategy for cancer therapy: nitric oxide donor as a therapeutic enhancer. Nitric Oxide. 2008; 19:205–216. [PubMed: 18503779]
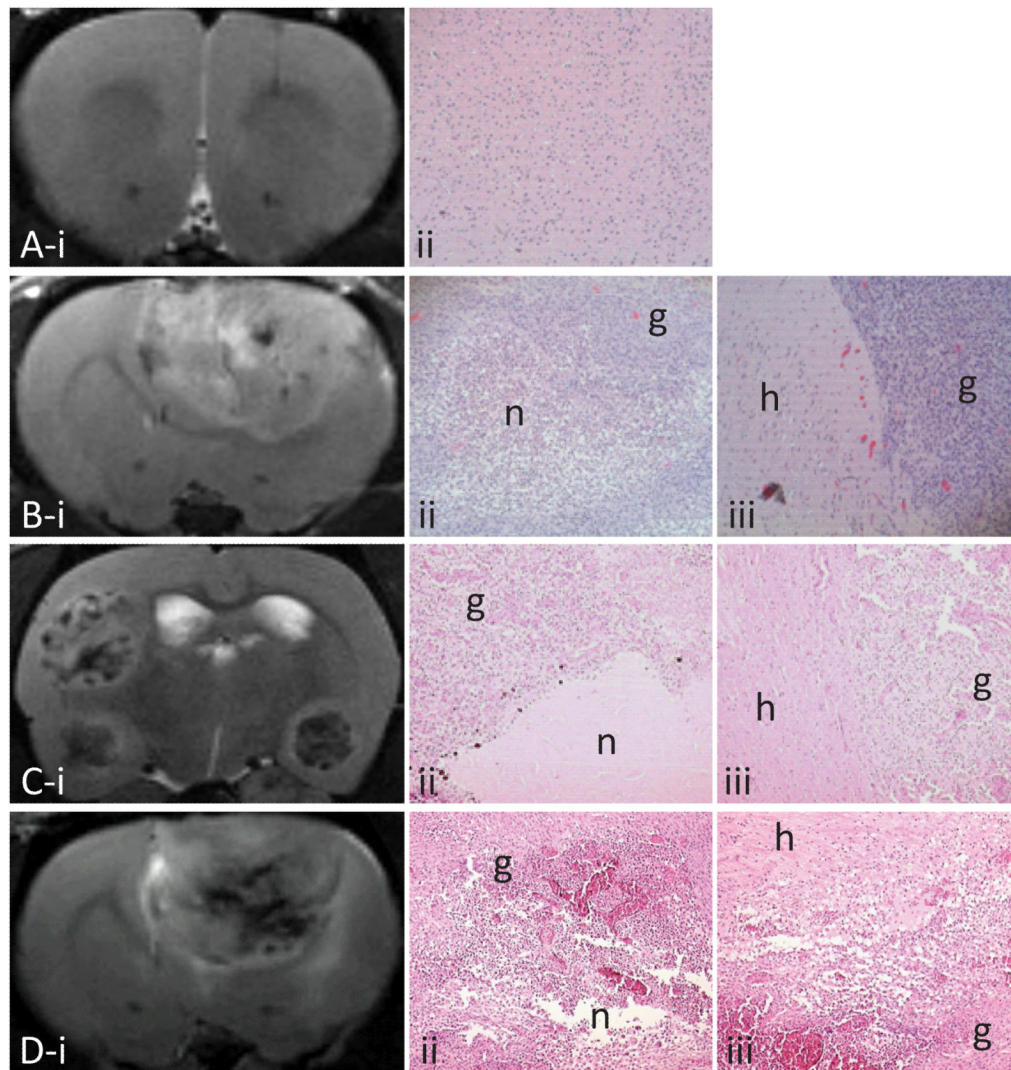
Figure 1.
Representative T$_2$-weighted images taken at various days after cell implantation (*panel i*) and corresponding H&E (x 10) showing necrotic (n, for areas of very low or null glioma cell density) and glioma tissue (g, *ii*) and the peritumoral region (healthy tissue, h, *iii*): rat injected with primary astrocytes at day 21 (*A*), C6 glioma at day 18 (*B*), ENU glioma at week 34 (*C*) and RG2 glioma at day 17 (*D*).
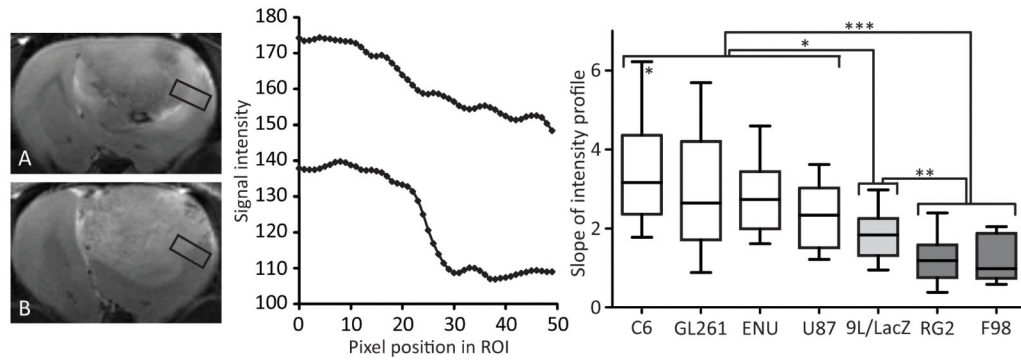
Figure 2.
T_2-weighted images of a RG2 (*panel A*) and C6 (*panel B*) gliomas, with corresponding pixel intensity profiles taken in the peritumoral region (a ROI is shown as a black rectangle). The slope between C6 tumor (high-intensity pixels) and healthy (lower intensity pixels) tissue is sharp (*bottom*), whereas an infiltrative RG2 glioma presents a more gradual intensity change (*top*). Panel C represents the slopes of the intensity profiles for each glioma model, calculated at the last MRI time point (about 23 days after cell implantation for the orthotopic implantation models and at 30 weeks of age for the ENU induction model). The data are represented as 10–90 percentile. (*) $p < 0.05$ between any glioma from the "white" group and the 9L/LacZ model, and between the C6 and the U87 models; (**) $p < 0.01$ between 9L/LacZ tumors and the tumors from the "dark grey" group; (***) $p < 0.001$ between the "white" and the "dark grey" groups.
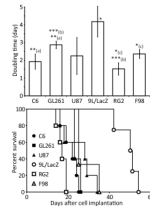
Figure 3.
Time needed by each glioma model to double in size (*top*) and survival curves of each group (*bottom*). The doubling time data are represented as the mean ± standard deviation. * p < 0.05 between the 9L/LacZ tumors and all other models, and between (c) the RG2 and the F98 gliomas; **(a) p < 0.01 between the C6 and the GL261 models; ***(b) p < 0.001 between the GL261 and the RG2 models. For the survival data, * p < 0.05 between the F98 and the C6 models, and between the F98 and the RG2 tumors; ** p < 0.01 between the 9L/LacZ gliomas and all other models.
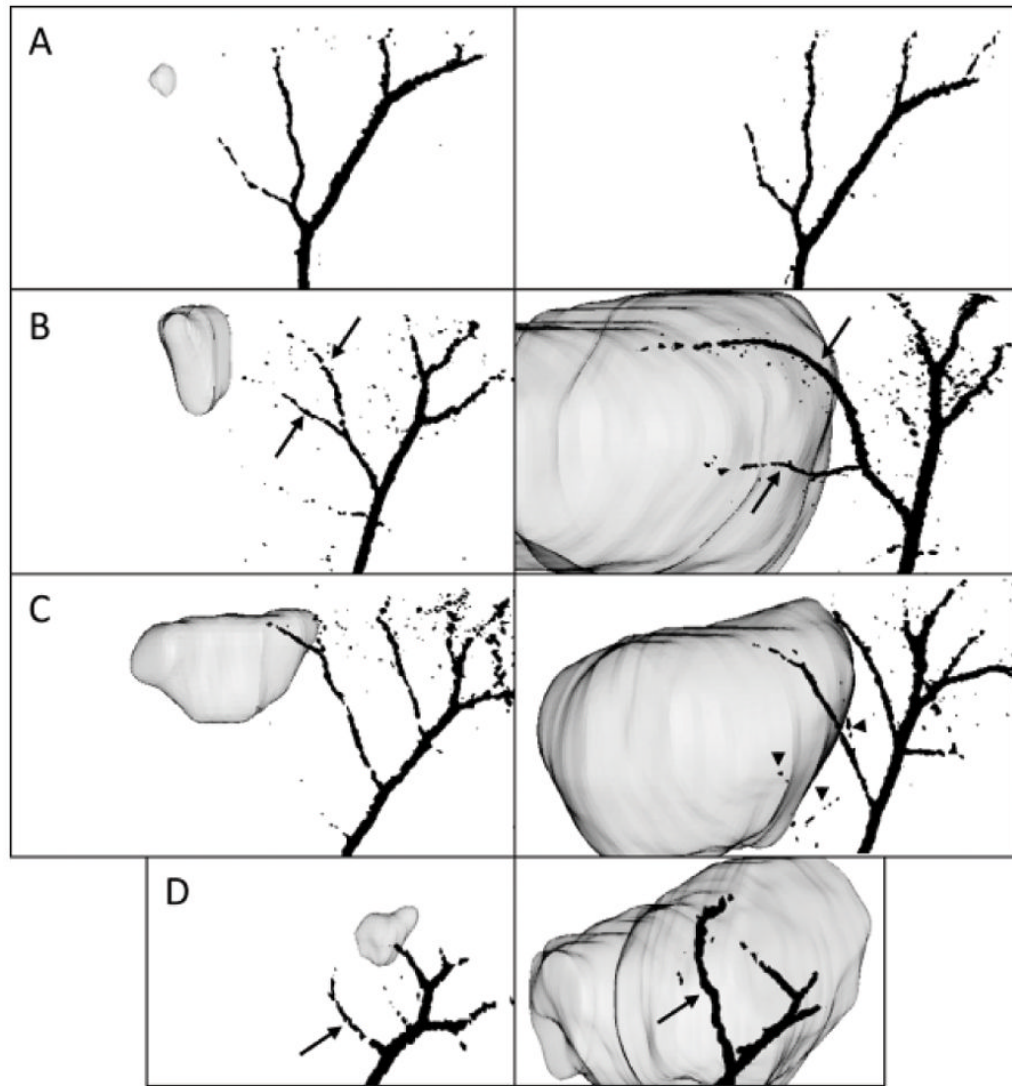
Figure 4.
3D vasculature representations were coregistered with the tumor, rending the ability to identify the altered pre-existing vessels (*black arrows*) and newly generated vessels (*arrowheads*). As shown here, they are taken at 30° from the sagittal plane of the brain, for an early and late time point and for representative glioma models presenting different angiogenic behaviors: primary astrocyte-implanted animal (panel A, day 7, *left*, and day 29, *right*), C6 (panel B, day 5, *left*, and day 21, *right*), U87 (panel C, day 7, *left*, and day 27, *right*) and GL261 gliomas (panel D, day 8, *left*, and day 23, *right*).
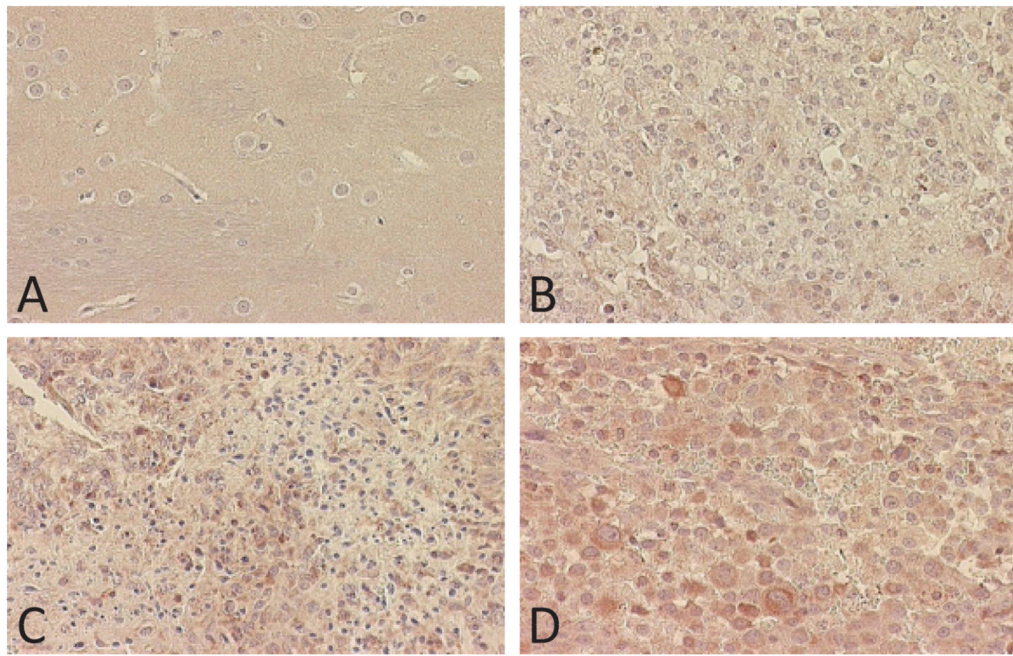
Figure 5.
VEGF staining (x 40) representative of normal brain tissue (A) and 3 glioma models: ENU gliomas (B), U87 gliomas (C) and RG2 gliomas (D).

Table 1

Vessel measurements

New blood vessels were counted and their length and diameter were estimated using the software Amira. Changes in the length and diameter of the pre-existing vessels proximal to the glioma were also calculated between the first and the last MRA time point (about 23 days after cell implantation for the orthotopic implantation models and at 30 weeks of age for the ENU induction model), and represented here as mean ± SD.

		CTRL	C6	F98	9L	GL261	RG2	U87	ENU
	Number	0	0	0	4±2*	2±1*	5±1.5*	5±1**	1±1
Newly observed vessels	Average length (μm)	-	-	-	1321	765	997	1126	1470
	Average diameter (μm)	-	-	-	68.5	74.5	69	65.4	81.3
Pre-existing vessels	Change in length (%)	−7±13	31±22***	94±75*	30±34*	41±81	8±25	24±58	19±40
	Change in diameter (%)	−7±11	40±23*, ***	45±52	18±25*	83±54**	4±45	8±16*	1±13

Number of new vessels:

*
$p < 0.05$ between the group of interest and the CTRL/C6 groups;

**
$p < 0.01$ between the group of interest and the CTRL/C6/F98/GL261/ENU groups.

Change in length:

*
$p < 0.05$ between the group of interest and the CTRL animals;

***
$p < 0.001$ between the C6 and the CTRL groups.

Change in diameter:

*
$p < 0.05$ between the C6 model and the GL261/RG2/U87 groups, between the 9L/LacZ and the CTRL groups, and between the U87 and the CTRL groups;

**
$p < 0.01$ between the GL261 model and the 9L/LacZ/RG2/U87 groups;

***
$p < 0.001$ between the C6 and the CTRL/ENU groups.